Mechanism of Crystal Formation in Ruddlesden-Popper Sn-Based Perovskites

Dong, Jingjin; Shao, Shuyan; Kahmann, Simon; Rommens, Alexander J.; Hermida-Merino, Daniel; ten Brink, Gert H.; Loi, Maria A.; Portale, Giuseppe

Published in:
Advanced Functional Materials

DOI:
10.1002/adfm.202001294

Publication date:
2020

ADVANCED FUNCTIONAL MATERIALS
www.afm-journal.de

Mechanism of Crystal Formation in Ruddlesden–Popper Sn-Based Perovskites

Jingjin Dong, Shuyan Shao, Simon Kahmann, Alexander J. Rommens, Daniel Hermida-Merino, Gert H. ten Brink, Maria A. Loi, and Giuseppe Portale**

Knowledge of the mechanism of formation, orientation, and location of phases inside thin perovskite films is essential to optimize their optoelectronic properties. Among the most promising, low toxicity, lead-free perovskites, the tin-based ones are receiving much attention. Here, an extensive in situ and ex situ structural study is performed on the mechanism of crystallization from solution of 3D formamidinium tin iodide ($FASnI_3$), 2D phenylethylammonium tin iodide (PEA_2SnI_4), and hybrid $PEA_2FA_{n-1}Sn_nI_{3n+1}$ Ruddlesden–Popper perovskites. Addition of small amounts of low-dimensional component promotes oriented 3D-like crystallite growth in the top part of the film, together with an aligned quasi-2D bottom-rich phase. The sporadic bulk nucleation occurring in the pure 3D system is negligible in the pure 2D and in the hybrid systems with sufficiently high PEA content, where only surface crystallization occurs. Moreover, tin-based perovskites form through a direct conversion of a disordered precursor phase without forming ordered solvated intermediates and thus without the need of thermal annealing steps. The findings are used to explain the device performances over a wide range of composition and shed light onto the mechanism of the formation of one of the most promising Sn-based perovskites, providing opportunities to further improve the performances of these interesting Pb-free materials.

1. Introduction

3D metal halide perovskite materials adopt an ABX_3 crystal structure, where A is occupied by either an organic or an inorganic cation, B is occupied by a divalent metal cation, and X is occupied by a halide anion.[1] This type of materials has superb properties such as good defect tolerance, long charge carrier diffusion length, and high absorption coefficient, which enable them to be ideal light harvesting materials in solar cells.[1–10] In particular, the lead halide based perovskite solar cells (HPSCs) have witnessed an unprecedented fast progress in their power conversion efficiency (PCE), which has reached a value of 25.2% in 2019 only after ten years of the beginning of the research activities.[11] However, the toxicity of lead causes concerns about the risk of environmental pollution. Substitution of Pb with a more environmentally friendly metal like tin (Sn) is one of the best options to solve this issue, as will allow retaining the main advantages of PSCs such as low-cost of the raw materials and of the fabrication methods, together with a high absorption efficiency in the thin films.[12] So far, the development of Sn-based PSCs lacks behind the Pb-based ones in terms of PCE and stability. The limiting factor for tin-based solar cells lie in the facile oxidation of tin and in the large number of tin vacancies.[13,14] Many strategies have been proposed to tackle these problems, including the use of antisolvent during thin film fabrication, changing of the organic cation or halide ligands and addition of 2D perovskite into the traditional 3D perovskite structure.[15–19] Recently, we have proven that adding a small amount of a long organic cation such as phenylethylammonium ($PEA^+ = C_6H_5(CH_2)_2NH_3^+$) to the 3D formamidinium tin iodide ($FASnI_3$) perovskite (in the following we will call this 2D/3D hybrid composition as Ruddlesden–Popper (RDP) phases) enhances the crystallinity and orientation of the 3D phase significantly, suppressing the tin oxidation and reducing the amount of tin vacancies. Consequently, the tin-based HPSCs using the RDP perovskite as light harvesting layer delivered a much higher PCE (9%) and stability compared to the pure 3D-based counterparts.[20,21] Key for achieving this high PCE value was a change in the film morphology together with the presence of a highly oriented layered

J. Dong, Dr. G. Portale
Macromolecular Chemistry and New Polymeric Material
Zernike Institute for Advanced Materials
University of Groningen
Nijenborgh 4, Groningen 9747 AG, The Netherlands
E-mail: g.portale@rug.nl

The ORCID identification number(s) for the author(s) of this article can be found under https://doi.org/10.1002/adfm.202001294.

DOI: 10.1002/adfm.202001294

Dr. S. Shao, Dr. S. Kahmann, A. J. Rommens, Prof. M. A. Loi
Photophysics and OptoElectronics
Zernike Institute for Advanced Materials
University of Groningen
Nijenborgh 4, Groningen 9747 AG, The Netherlands
E-mail: M.A.Loi@rug.nl

Dr. D. Hermida-Merino
DUBBLE CRG BM26@ESRF Netherlands Organization for Scientific Research (NWO)
71 Avenue des Martyrs, Grenoble 38000, France

G. H. ten Brink
Nanostructured Materials and Interfaces
Zernike Institute for Advanced Materials
University of Groningen
Nijenborgh 4, Groningen 9747 AG, The Netherlands

RDP structure. These results indicate that the importance of the crystallization and structure control on the performances of the tin perovskite solar cells.

In order to provide guidance to further improve the performance of the tin-based solar cells, knowledge of the mechanism and stages of crystal formation that occur during solvent evaporation is crucial to optimize the structure of these materials. Film formation plays a critical role in this field as the perovskite film structure and morphology are highly sensitive to the processing parameters.[12,22–24] The film formation process is relatively well-studied for Pb-based perovskites and a certain number of in situ studies of the structural evolution during the fabrication of thin films recently appeared. Among various techniques, time-resolved grazing incidence wide-angle X-ray scattering (GIWAXS) is a mature and powerful one to study the structural transitions occurring in perovskite materials during printing, spin coating and during temperature annealing.[25–27] Poister et al. monitored changes in the formation of crystalline phase under varying process conditions in real-time during film growth by X-ray diffraction and revealed the importance of post annealing treatment.[22] Hu et al. revealed the material transformation pathways and the morphology formation mechanism of Pb-based perovskites from precursor solution to polycrystalline films over relevant temperature and time scales by using 2D grazing incidence x-ray diffraction (2D-GIXD). The existence of intermediate structures comprised of an octahedral $[PbI_6]^{4-}$ center surrounded by cooperative ions was proved.[24] Schlipf et al. also confirm the power of GIXD by a real-time study on the Pb-based RDP perovskite thin films and revealed the formation mechanism.[23] These works showing the evolution of Pb-based perovskite materials at the nano/meso scale offered important insights into the crystallization kinetics and material transformation, and clarified crucial steps to obtain high-quality Pb-based perovskite thin films. Despite the large number of in situ studies about crystallization mechanisms in Pb-based perovskites, detailed studies on the structural transformations occurring in Sn-based perovskites are lacking up to now.

In order to fill this gap, here we report the structural evolution of $FASnI_3$, PEA_2SnI_4, and RDP mixed dimensional hybrids (schematic crystal structure shown in Figure S1 in the Supporting Information) during spin coating from a DMF:DMSO mixture at room temperature by using ex situ and in situ grazing incidence wide-angle X-ray scattering. Using variable angle ex situ GIWAXS in combination with SEM and photoluminescence data we study the morphology, the crystal orientation and the layered structure of the 2D/3D mixed hybrid perovskites. In situ GIWAXS is instead used to study the formation mechanism of the Sn-based hybrid perovskite thin films. Our results show that, similarly to Pb-based perovskites, precursors are formed before crystallization sets in. However, contrary to what commonly reported for Pb-based perovskites, direct transition to the crystalline state from the disordered precursors is observed at ambient temperature, without formation of intermediate ordered phases. Most importantly, our results demonstrate that crystallization always tends to start at the air/solution interface and coordination of the long organic cations around the growing crystals is key to obtain good crystal orientation. Analysis of the kinetic of crystallization shows how the mechanism of crystal growth is changed upon the long organic cation addition from a 3D to a 2D crystal growth mode. These features allow the tin-based system to form ordered perovskite structures directly after spin coting, without the need of further annealing.

2. Results and Discussion

2.1. Ex Situ Study

Before investigating the structural evolution of the perovskite thin films in situ, we have performed a detailed structural characterization of the final film structure for the Sn-based perovskites using ex situ GIWAXS, SEM and photoluminescence (PL). Thin films of pure 3D $FASnI_3$, pure 2D PEA_2SnI_4 and RDP with a nominal formula of $PEA_2FA_{n-1}Sn_nI_{3n+1}$, where n is the theoretical number of inorganic octahedral layers separated by double layer of PEA cations, have been prepared by spin coating without (**Figure 1**a, top row) and with (Figure 1a, bottom row) sequential antisolvent treatment process (see experimental section for details). Figure S2a (Supporting Information) shows typical GIWAXS images of RDP $n = 8$ without antisolvent addition where the main peaks that will be discussed here are labeled.

As shown in Figure 1a, the pure 3D sample has an almost isotropic structure, with Debye-Scherrer rings occurring at positions that agree with a randomly oriented orthorhombic (space group *Amm*2) crystal structure with cell $a \times b \times c$ = 6.35 Å × 8.95 Å × 9.1 Å, expected for the $FASnI_3$ perovskite[23] and in agreement with what was reported previously for thin films.[21,28,29] However, a more careful look shows the presence of a weak orientation, attributed to some texture of the crystalline structure resent at the air/film interface. This aspect will be discussed in more details below in the in situ section. On the contrary, the pure 2D material with $n = 1$ shows a very high degree of order and high orientation, especially when processed with antisolvent. The structure of the PEA_2SnI_4 can be indexed using the reflections from a monoclinic unit cell (space group *C*2/*m*) with lattice parameters $a \times b \times c$ = 32.5 Å × 6.1 Å × 6.1 Å, β about 92° and the *h*00 planes highly aligned parallel to the substrate, typical for the layered perovskite.[30] Parallel here means that the extended inorganic slabs composed by the tin iodide octahedron are parallel to the substrate.

As reported previously for both Pb-based and Sn-based perovskites, incorporation of small fractions of long organic cations commonly used for the preparation of so-called 2D perovskites strongly promotes formation of highly oriented perovskite crystallites with same orthorhombic 3D crystal structure, beneficial for the efficiency of photovoltaic devices.[21,31,32] Depending on the processing conditions used here (ambient temperature, DMF:DMSO as solvent and spin coating rate of 2000 rpm), a strong influence on the thin film crystallite orientation is visible for $n < 24$. In general, the addition of PEA promotes growth of orientated crystallites independently of the processing parameters, as evidenced by the fact that isotropic diffraction rings are substituted by diffraction arcs in the GIWAXS patterns. All the diffraction arcs at high angles can be indexed according to the expected reflections from an oriented phase with unit cell virtually identical to the one for the 3D $FASnI_3$ structure (see Figure S2a in the Supporting Information) oriented with

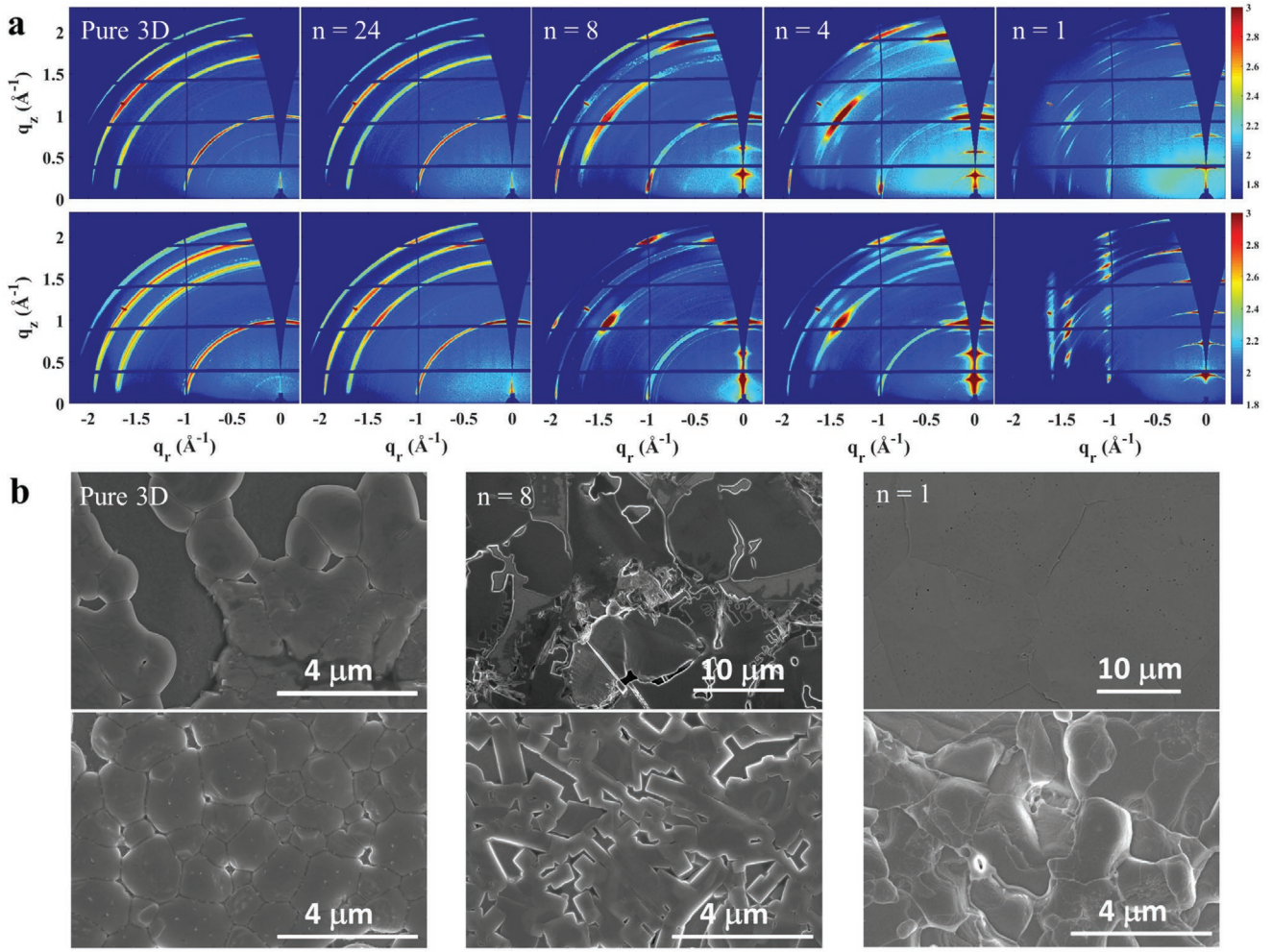

Figure 1. a) GIWAXS images of the pure $FASnI_3$ 3D, RDP hybrid perovskites with $n = 24$, 8, and 4 and the pure 2D perovskite ($n = 1$) thin films processes without (top row) and with (bottom row) antisolvent. Note that some images (i.e., pure 3D w/o antisolvent and $n = 8$ w antisolvent) show some additional isotropic weak peaks originating from the material spilled on the spin coater chamber windows and obviously are not related to the thin film structure. b) SEM images of the surface for the pure 3D, RDP $n = 8$, and pure 2D $n = 1$ thin films processed without (top row) and with (bottom row) antisolvent. For $n = 8$ and $n = 1$ processed without antisolvent the grains are so large that we have preferred to show SEM images using a larger magnification (scale bar of 10 μm).

the 100 planes parallel to the substrate. When the content of PEA is increased, formation of RDP phases with high n (well above 5) is expected.[33] In this case, the reflections expected for the RDP phase appear at positions similar to the ones for the 3D phase and consistent with our GIWAXS patterns, provided that the RDP crystals are oriented with their 001 (or 101) planes aligned parallel to the substrate, that is with the inorganic slabs perpendicularly oriented with respect to the substrate (peak indexing for the RDP phase is reported in Figure S2a in the Supporting Information).[33] The crystallite orientation is consistently better for the thin films processed using the antisolvent treatment. For $n = 8$ and $n = 4$ samples, clear low angle peaks can be observed along the q_z direction, indicative of an additional 2D layered phase. The location of these peaks is different from the location of the *h00* peaks in the pure 2D PEA_2SnI_4 perovskite. Figure S2b (Supporting Information) shows the plot of the line cuts along the q_z direction for the samples reported in Figure 1a. Though the *200* peak of the pure 2D with $n = 1$ is located at 0.39 $Å^{-1}$, this peak is located at around 0.3 $Å^{-1}$ for both $n = 4$ and $n = 8$ samples. The q values of the observed *h00* reflections for this quasi-2D phase suggest that a RDP phase with $n = 2$ is formed, in agreement with what was reported previously.[21] Peak indexing of this RDP $n = 2$ phase suggests a monoclinic unit cell (space group *C2/m*) with lattice parameters $a \times b \times c = 41.5$ Å × 6.2 Å × 6.2 Å, β about 91° and the *h00* planes highly aligned parallel to the substrate (see Figure S2c in the Supporting Information). Hereafter, we will refer to this RDP $n = 2$ phase as quasi-2D.[21] Interestingly, the location of the quasi-2D first order reflection is independent from the content of the low-dimensional component added to the solution. This indicates that this phase may have higher stability with respect to other phases with higher n and will be formed preferentially with the processing conditions used here. In a very recent work, Soe et al. reported the hybrid Pb-based perovskite packing preference with a calculation of enthalpy of formation of the $(BA)_2(MA)_{n-1}Pb_nI_{3n+1}$ series as a function of

the perovskite layer thickness (n).[34] They found that $n = 2$ and 4 could have the most negative Gibbs free energy of formation indicating that they are the most thermodynamically stable. It seems that the quasi-2D with layer number equals to 2 is the dominant structure for Sn-based systems.

Interestingly, the thin films with $n = 4$ exhibit the coexistence of more phases, along with the oriented crystals with 3D-like crystal structure and the quasi-2D phase. For instance, the RDP with nominal $n = 4$ sample clearly shows extra peaks that can be attributed to a small fraction of a higher n (5) RDP phase with preferred vertical orientation (c axis parallel to the substrate; see Figure S2c in the Supporting Information for more details).[19,30]

Figure 1b shows scanning electron microscope (SEM) images of pure 3D, RDP $n = 8$ and pure 2D $n = 1$ perovskite thin films. For all the three studied samples, the observed grain size is much smaller and the film is more homogenous when antisolvent is used. This is due to the increased nucleation rate and speed up of crystallization caused by antisolvent injection.[35] Moreover, addition of the 2D component to the system causes a change in the grain morphology and the RDP $n = 8$ film processed with antisolvent has small non-spherical grains with blurred boundaries, in agreement with SEM images for the $n = 24$ hybrid film reported elsewhere.[21] We also observe some pinholes for RDP $n = 8$ which could relate to the structure reported by Chen et al.[29] Here is important to underline that the morphology of most of the samples in the bottom row of Figure 1b is substantially worse than the one we have reported earlier.[21] The reason for this difference is that in the manuscript of Shao et al., a much higher spin-coated speed was used than in this work (4000 rpm vs 2000 rpm). The limited spin-coated speed used here is due to the equipment used for the in situ experiment.

An important aspect of these tin RDP hybrid perovskite thin films is the location of the 2D phases inside the film and their orientation. These two factors seem to be affected by the processing method and the substrate of choice.[33,36] For instance Liao et al. reported a vertical growth on NiO_x substrate of thin perovskite domains with the 2D component (PEA) mainly located at the boundary of the 3D perovskite crystal grains,[33] while on the similar system, but with lower amount of the 2D component, Wang et al. reported the location of the 2D at the air/film interface.[36] In order to understand where the 2D phase is located in our films, we have thus performed GIWAXS analysis at different incident angles to probe the structure close to the air/film interface and deeper into the bulk of the film (see **Figure 2**). When the region close to the air/film interface of the thin film is illuminated ($\alpha_i = 0.17°$, equal to the estimated critical angle for $FASnI_3$ and nominal penetration depth ≈10 nm[21]), the RDP hybrid film with $n = 8$ processed without antisolvent (Figure 2a) shows a weak peak associated to the 1st order reflection of the quasi-2D structure indicated by white arrow) together with the diffraction peaks for the oriented 3D-like phase. Conversely, the 1st and 2nd order reflections of the quasi-2D structure are much stronger and clearly visible when $\alpha_i = 1.4°$ (nominal penetration depth ≈30 µm) is used. For the film treated with the antisolvent, the peaks of the quasi-2D phase are only detected at $\alpha_i = 1.4°$, while no trace of the quasi-2D structure is observed at $\alpha_i = 0.17°$. Looking at the very narrow angular spreading of the quasi-2D GIWAXS peaks

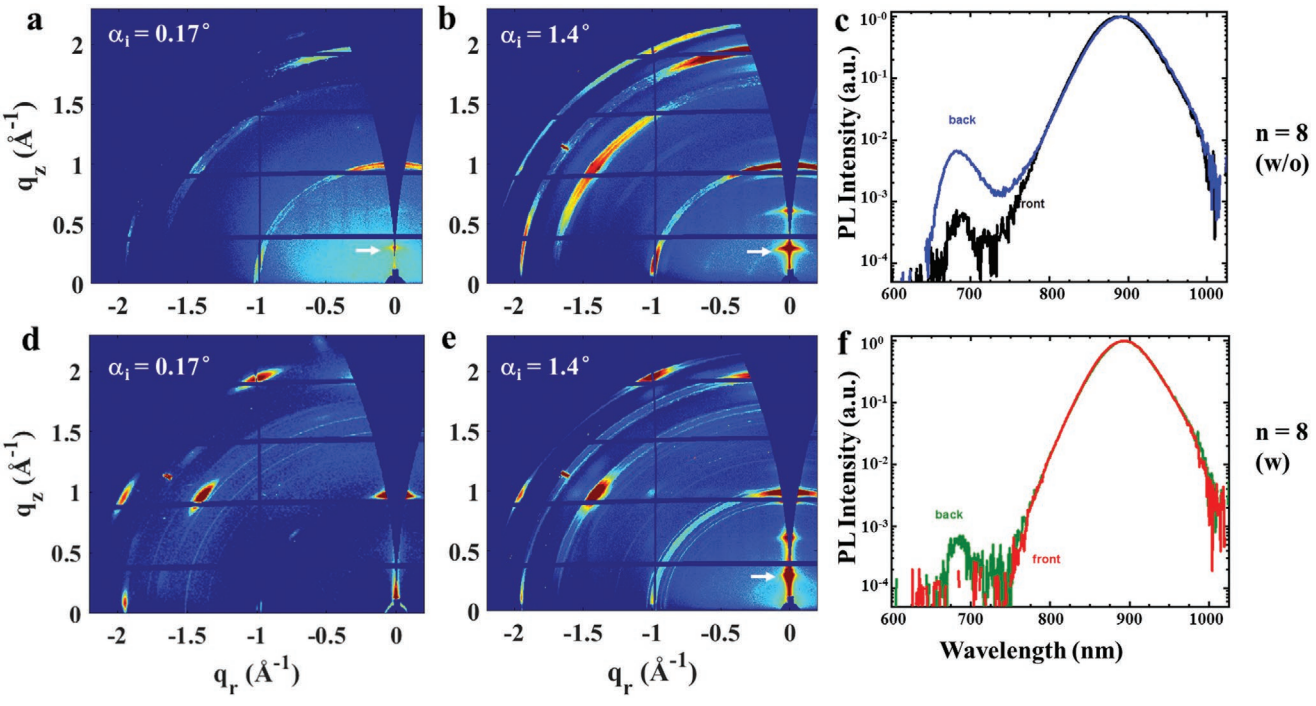

Figure 2. Evolution of the GIWAXS patterns and PL spectra for the hybrid RDP thin films $n = 8$ processed without (top line) and with antisolvent treatment (bottom line). The GIWAXS patters were recorded using $\alpha_i = 0.17°$ a,d) and 1.4° b,e). The white arrow highlights the position of the *100* reflection of the quasi-2D phase located at the substrate/film interface. Steady state PL intensity for both front side and back side illumination measurements performed in films processed without c) and with antisolvent f).

strongly focused along the q_z vertical direction, we can conclude that the structure is strongly aligned with the *h00* planes (i.e., with the inorganic slabs) parallel to the substrate. To further confirm the location of the quasi-2D phase within the thin films, PL spectra were acquired upon selective illumination of the front side and the back side (Figure 2c,f). When exciting on the back side, two separated emission bands can be observed at around 680 and 900 nm, indicative of the quasi-2D ($n = 2$) and the 3D structure, respectively (see Figure S3 in the Supporting Information for the PL spectra of the pure materials). Corresponding time-resolved data shown in Figure S4 (Supporting Information) underlines the previously discussed beneficial effect of PEAI addition on the carrier lifetime,[8,20] but shows no major difference on the carrier lifetime for the front and back side. In line with the GIWAXS results, for both films, the PL spectra of the front side show a much weaker intensity of the 2D band, and the 2D signal at 680 nm is completely absent in the PL spectra of the front side of the $n = 8$ film processed with antisolvent (red curve, Figure 2f). Thus, the GIWAXS and PL results clearly demonstrate that the quasi-2D phase is located at the bottom of the film, in contact with the substrate.

2.2. In Situ Study

Next, we investigated the mechanism of formation that brings the RDP hybrid Sn-based perovskites to adopt the observed layered structure, as well as the mechanism of formation of the pure 3D and pure 2D perovskite thin films during spin coating by in situ GIWAXS. A home built on line spin coater used for previous in situ GISAXS experiments[37,38] was equipped with a remotely controlled injection system able to sequentially dispense two different solutions under N_2 gas inert atmosphere (Figure S5, Supporting Information). The spin coating experiments have been performed at 2000 rpm, without and with antisolvent injection. In the first case, natural evaporation of the DMF:DMSO solvent was followed for a period up to 30 min from the start of the spin coating, due to the slow solvent evaporation. On the contrary, when antisolvent injection was used, few minutes were sufficient to complete the spin coating process and the film formation was followed for 10 min.

Figure 3a–c shows the evolution of the integrated GIWAXS intensity $I(q)$ as a function of the modulus of the scattering vector q and the drying time. The integrated intensities of the main crystalline reflections for the pure 3D, RDP $n = 8$ and pure 2D ($n = 1$) samples processed without antisolvent injection are reported in Figure 3d–f. Similarly, the GIWAXS intensity evolution over q and time when antisolvent addition is used are presented in Figure S6 (Supporting Information). Figure 3a–c shows that perovskite crystallization generally starts shortly after the beginning of spin coating, shortly above 100 s. However, before the crystalline diffraction peaks appear, two broad signals are visible. For the pure 3D DMF:DMSO solution, these two broad peaks are located around 0.5 and 1.7 $Å^{-1}$ (Figure 3a). Similar broad reflections have been first observed by Hu et al. for Pb-based $MAPbI_3$ perovskites and they have been associated to the formation of intermediate $[PbI_6]^{4-}$ cage-like structures during hot printing from solution.[24] More recently, similar structures have been reported by Zhang et al. during the complex drying process that goes through formation of disordered sol–gel precursors, intermediate phases, and ultimately perovskites.[39] These disordered precursor often evolve into ordered intermediate phases mainly constituted by PbI_2 coordinated by DMF or DMSO.[40] It was demonstrated that control over these intermediate phases is crucial for optimizing the final optoelectronic properties.[34,41,42] Considering the broad nature of these observed peaks preceding crystallization, we can infer that similar disordered precursors also exist in the Sn-based perovskite solution used here and they play a crucial role during the crystallization of $FASnI_3$ perovskites. Similar precursors exist also for the pure 2D and the RDP systems. In fact, the presence of two broad reflections observed in Figure 3b,c before crystallization certifies the appearance of a similar disordered precursors also for the RDP hybrid solutions and for the pure 2D $n = 1$ solution. However, the structure of these precursors seems to be affected by the presence in solution of the longer organic cation (PEA^+). In Figure 3g we have plotted the integrated GIWAXS intensity for the three precursor solutions at t = 100 s, before the start of crystallization. Some important differences are noticeable. First, the scattering intensity of the precursors in the pure 2D $n = 1$ solution is much higher than in the pure 3D solution. Second, the position of the first broad peak is significantly shifted to lower scattering angles for pure 2D $n = 1$ intermediate ($q = 0.43$ $Å^{-1}$) as compared to the pure 3D ($q = 0.57$ $Å^{-1}$) suggesting that the precursor structure in the low-dimensional 2D perovskites is larger than the 3D ones. Third, the width of the first peak of the pure 2D $n = 1$ intermediate is sensibly sharper than the one for the pure 3D, pointing to a more efficient packing of these intermediates, reflecting the high order of the 2D perovskite thin films. Interestingly, in the hybrid RDP $n = 8$ precursor solutions, the precursors adopt a structure that is again different with respect to the pure 3D and pure 2D ones. The first peak of the disordered precursors in the RDP $n = 8$ solution show intensity and position in between the values of the pure 3D and pure 2D $n = 1$. The second peak at high scattering angles shows a much higher intensity. These observations suggest that the FA^+ and PEA^+ organic molecules participate in the coordination shell of the disordered precursors. The way these precursors evolve over time is also different depending on the low-dimensional component content in solution. The scattering intensity of the precursors in the pure 2D $n = 1$ solution is lower at first when compared to that of the pure 3D counterpart and undergoes a significant increase during drying. The maximum intensity for the 2D disordered precursor is located at 140 s, which is significantly later than for the pure 3D (110 s). This suggest that a larger degree of supersaturation is needed for the 2D structure to be formed with respect to the 3D structure.

At about $t = 110$ s for pure 3D, 120 s for RDP $n = 8$, and 140 s for the pure 2D, crystallization sets in. The scattering intensity from the precursors starts to drop dramatically and the diffraction signals typical for the corresponding perovskite crystalline structures appear and grow over time (see Figure 3d–f). The primary crystallization process is completed within about 200 s from the onset of crystal formation for the pure 3D and within about 100 s for the RDP $n = 8$ and the pure 2D samples, exactly matching the time needed for the precursors to disappear. This means that the disordered precursors directly convert into the

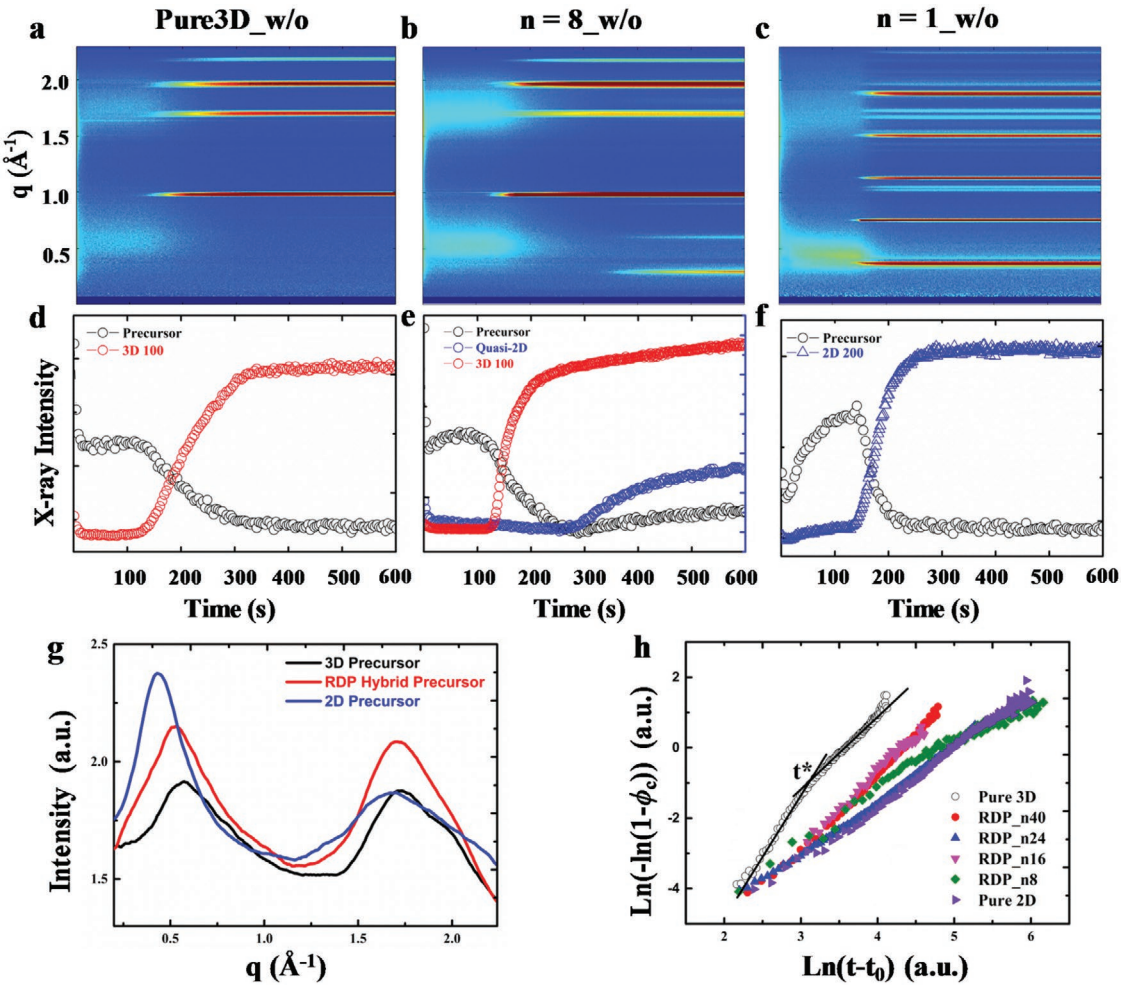

Figure 3. Time evolution of the integrated GIWAXS profiles (top row) and the integrated peak intensities (middle row) for the pure 3D a,d), RDP $n = 8$ b,e) and pure 2D $n = 1$ c,f) samples processed without antisolvent injection. The diffraction signals followed are the 1st peak of the precursor structure, the 100 reflection of the 3D phase, and the 200 peak of the quasi-2D and pure 2D phases. g) GIWAXS intensity for the intermediate states of the pure 3D (black), RDP $n = 8$ (red), and pure 2D (blue) perovskite films and h) Avrami plots of the main peaks of different samples. A logarithmic intensity scale between 1 and 4 was used for (a)–(c).

crystalline structure without forming other ordered solvated intermediate phases. This is quite different from what was observed for $MAPbI_3$ and $(BA)_2(MA)_3Pb_4I_{13}$ films when spin coated at ambient temperature, where thermal annealing is needed to activate organic cation intercalation into the solvated ordered PbI_2 precursors.[40,43] We can attribute this specific behavior to the very fast crystallization of Sn-perovskites at room temperature.[44] Indeed, this fast crystallization leads to large and inhomogeneous grain size with poor coverage of the substrate as evidenced by SEM (Figure 1b). Using the antisolvent compensates for this effect by dramatically increasing the nucleation and growth rate, allowing to obtain more uniform film morphologies (Figure 1b).

A striking observation was revealed by the in situ GIWAXS experiments on the RDP $n = 8$ solution both with and without antisolvent addition (Figure 3b; Figure S6b, Supporting Information). Unexpectedly, the appearance of the quasi-2D phase in the hybrid RDP perovskites is observed with a substantial delay with respect to the appearance of the crystalline 3D phase. In particular, the quasi-2D phase crystallizes when the crystallization of the oriented 3D phase is almost completed (Figure 3e). Thus, contrary to what could be thought, the reason for the enhanced thin film orientation observed in Figure 1 for the mixed dimensional Sn-based perovskites is not the templated growth of the 3D structure from the already formed quasi-2D phase. The crystallite orientation observed here seems rather to be a consequence of the crystal growth on nuclei formed at the air/solution interface, as will be discussed in detail below and in opposition to the templated-aided growth from the substrate recently reported for Pb-based perovskite deposition on preheated substrates.[40]

As already mentioned, a different evolution of the GIWAXS integrated intensity is observed when comparing the kinetics of the pure 3D and 2D phases, with the pure 2D phase showing faster temporal evolution (Figure 3d,f). In order to learn more about the possible mechanism of the nucleation and crystallization in the pure and hybrid films, we have conducted Avrami analysis of the crystallization behavior for all the analyzed

samples. Strictly speaking, the spin coating process is not isothermal. However, Avrami analysis can be successfully carried out to gain insights on the crystallization mechanism acting during drying.[45] According to the Avrami model, the evolution of the crystalline phase can be described as:

$$\phi_c = 1 - \exp\left(-kt^m\right) \quad (1)$$

where ϕ_c is the crystallinity, k is a constant dependent upon nucleation and growth rate, and m is the kinetic exponent related to the type of nucleation and growth geometry.[46–48] In order to extract the values of k and m for the different samples, linear fits of the curves in the $\ln[-\ln(1-\phi_c)]$ plot reported in Figure 3h were performed. The kinetic parameters calculated according to the Avrami equation are reported in Table S1 in the Supporting Information. Inspection of Figure 3h shows a remarkable difference in the crystallization mechanism between the pure 3D and pure 2D $n = 1$ Sn-based perovskites. Generally, the curve for pure 3D sample shows a clear reversal point in the Avrami exponent and the corresponding rate constants. A change from an initial process with $m \approx 3.2$ to a second one with $m \approx 2.2$ is observed. According to Hulbert and Bart's theory,[49,50] these results suggest that, in the pure 3D solution, the system undergoes first a phase boundary controlled 3D growth process with a deceleratory growth rate, followed by a secondary diffusion controlled crystallization process occurring at the crystal grain boundary area. This conclusion is in agreement with the grain morphology observed by SEM. Additional information on the nucleation and growth mechanism of the pure 3D system can be retrieved by observing the GIWAXS patterns at selected drying time that are reported in Figure S7 (Supporting Information). By comparing the GIWAXS pattern of the pure 3D film processed without antisolvent 25 s after the onset point ($t \approx 135$ s) with the patterns at intermediate time ($t = 200$ s) and at finishing time ($t \approx 300$ s), we can observe how the first crystals formed in the early stage of crystallization exhibit significant orientation (highlighted with a white arrow). During drying, the overall orientation decreases as the newly formed crystals grow without a specific orientation. In Figure S7j (Supporting Information), we plot the GIWAXS pole figures for the *100* reflection against the azimuthal angle φ, where a clear trend can be observed as the peak width becomes broader over time. Thus, the first nuclei are most probably formed at the air/solution interface and crystallite with significant preferential orientation grow via heterogeneous growth. This could be the result of the fast DMF evaporation at the surface of the wet layer causing the air/solution interface to reach supersaturation first.[29,51] Recently, other works also reported about dominant surface crystallization in perovskites.[29,52] However, for the pure 3D solution, significant bulk crystallization is present and nucleation and growth of crystals from the precursor solution occurs inside the wet layer as well, leading to randomly packed crystallites. Interestingly, we found that at the beginning of the crystallization the *100* peak is mainly oriented along the azimuthal angle $\varphi = 145°$ which indicates that the *h00* planes are not parallel to the substrate. The surface and bulk crystallization both contribute to the first stage observed in the Avrami plot. Over time the crystallites grow and will tend to impinge among them. Further secondary crystallization occurs in the space between crystals at the grain boundary which provides the second stage observed in the Avrami plot of the pure 3D. The mechanism of crystal formation for the $FaSnI_3$ sample is summarized in the top row of **Figure 4**.

On the contrary to what is observed for the pure 3D, a single stage of growth is observed for the pure 2D sample, suggesting that the nucleation and growth rates are approximately constant during solvent evaporation (Figure 3h). A single Avrami exponent of $m \approx 1.6$ is extracted, which suggests a diffusion controlled 2D growth mode with a deceleratory growth rate.[49,50] Thus, in the pure 2D solution, and crystallization occurs first at the air/solution interface and proceeds from top to bottom toward the solution/substrate interface and without significant bulk crystallization that would lead to random orientation, in agreement with what reported for Pb perovskites.[29] The initial orientation is thus maintained during the crystallization, leading to high orientation of the 2D thin films with the inorganic slabs parallel to the substrate. This process is depicted in the second row of Figure 4.

Interestingly, addition of different amounts of the low-dimensional components to the 3D solution readily affects the crystal growth. A transition from 3D growth mode to 2D growth mode is observed. As shown in Figure 3h, the Avrami plots for all the 2D/3D mixed dimensional samples ($40 \leq n \leq 8$) all lie in between the pure 3D and the pure 2D, but closer to the one of pure 2D. The calculated Avrami exponent m progressively decreases from 2.2 for $n = 40$ to 1.6 for $n = 8$, as shown in Table S1 (Supporting Information). The first crystals that form in the hybrid systems are rather oriented with their *h00* planes parallel to the substrate, that is the *h00* reflections aligned at $\varphi = 90°$ (Figure S7, Supporting Information; rather than at $\varphi = 145°$, as in the pure 3D case. However, for $n \geq 24$ bulk crystallization is still important and randomly oriented crystals grow from the bulk precursor solution (Figure S7d–f, Supporting Information). For $n \leq 8$, bulk crystallization is mostly suppressed and heterogeneous growth of nuclei at the air/solution interface region is the predominant process leading to strongly oriented crystals (see Figure 1a and Figure S7g–i in the Supporting Information). The same analysis of the time evolution of the perovskite film formation was conducted when antisolvent treatment is applied (Figure S6, Supporting Information). As soon as the antisolvent is injected crystallization starts due to rapid supersaturation. Similar features observed for the thin films obtained without antisolvent are found. The obtained crystal structure at the end of the spin coating is the same, independently if antisolvent was used or not. Formation of the quasi-2D phase is again observed with a significant delay and starts after the main 3D crystallization almost finished. Avrami analysis was also conducted when the antisolvent treatment is used, although the available data points are limited due to the very fast crystallization kinetics. The kinetic exponent of pure 3D with antisolvent and RDP $n = 8$ with antisolvent are found to be 1.9 and 1.1, respectively. This indicates that the addition of the antisolvent accelerates the nucleation rate to an instantaneous mode, but without changing the 3D growth mode of the pure 3D film and the 2D growth mode of RDP hybrid films.[49] However, the much higher nucleation rate induced by the antisolvent results in a significantly smaller domain dimensions as observed above by SEM images reported in Figure 1.

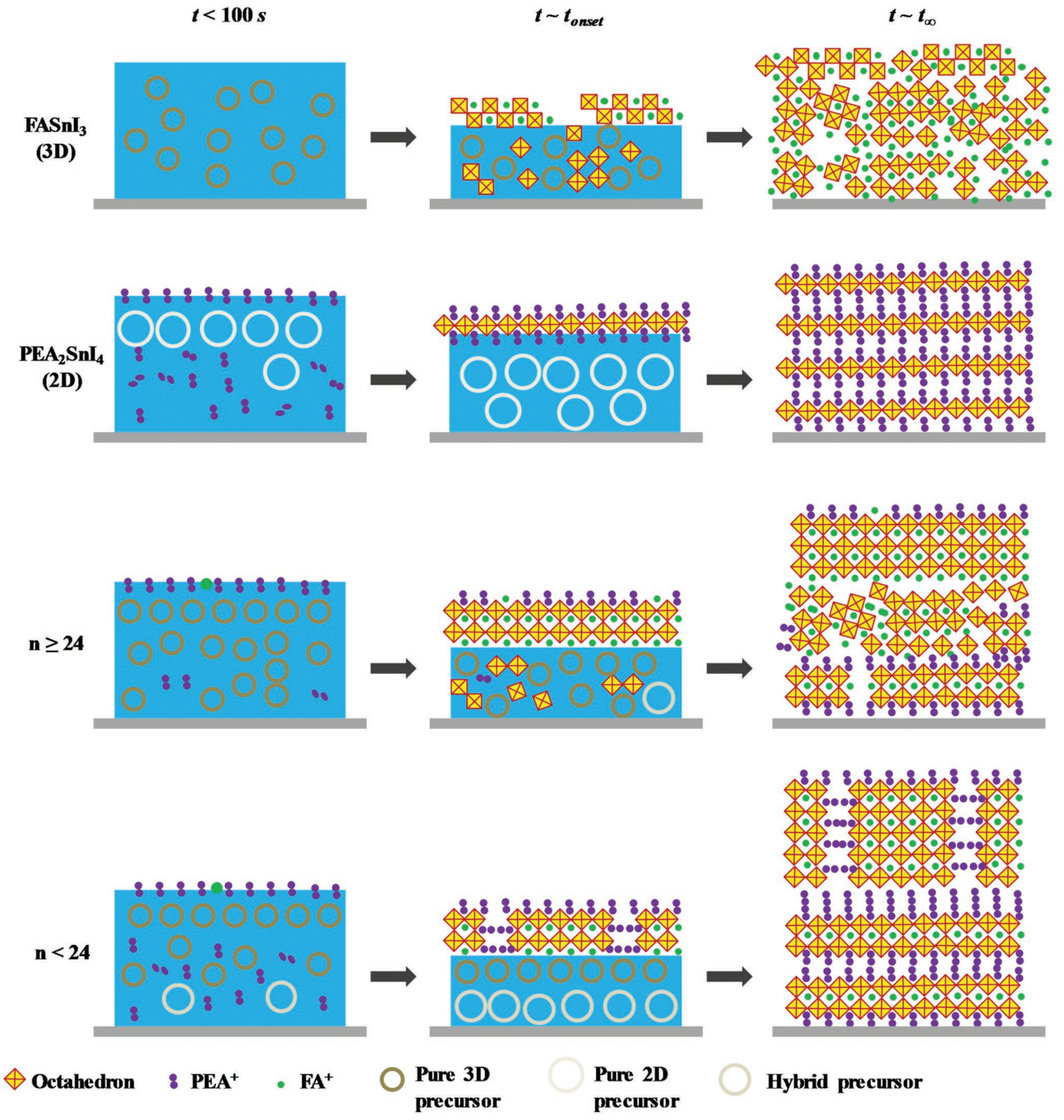

Figure 4. Proposed mechanism of thin films formation for spin-coated Sn based perovskite. Note: Due to the image scale consideration, the final state of hybrid film is not based on the real ratio between 2D and 3D component.

Considering the in situ GIWAXS results, it appears clear that the presence of the PEA^+ in solution is responsible for the induced orientation of the RDP tin perovskites. During the early stages of crystallization, PEA^+ cations coordinate to the periphery of tin halide octahedron precursors and later to the edges of the growing crystals, pointing toward the surrounding solution and (possibly) toward the air. This is in line with recent reports about the formation of a more hydrophobic surface responsible for increased humidity resistance in RDP Pb-based perovskites.[53] The PEA^+ coordination on the crystal surfaces may force the alignment of the initial crystals with the *100* planes parallel to the surface. Considering the high fraction of the FA molecules with respect to the PEA ones for most of our samples, supersaturation is reached early for the $FASnI_3$ and a surface layer of the pure 3D perovskite grows first. This is also favored by the fact that the 3D precursors develop more rapidly

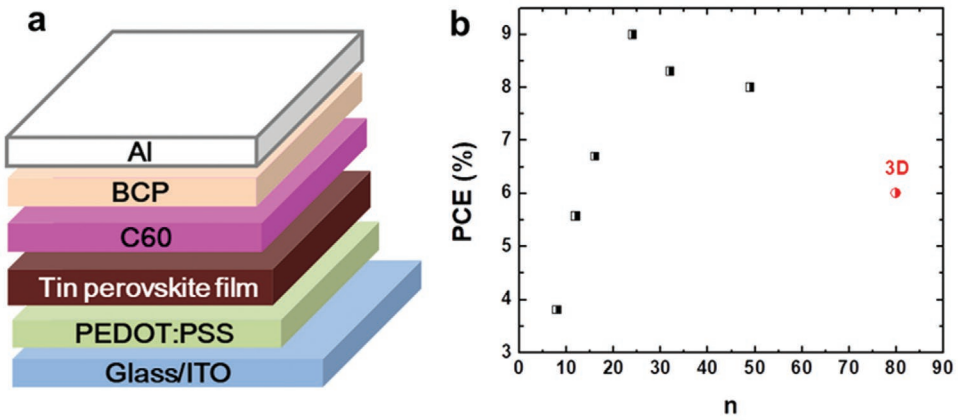

Figure 5. a) Device structure and b) steady-state PCE tracked at the maximum power point of the $PEA_2FAn_{-1}SnnI_3n_{+1}$ devices with different *n* numbers.

than the 2D ones (Figure 3d,e). With time, FA^+ and tin iodide are continuously added to the growing layer and the solute concentration in the bottom region increases until supersaturation for the low-dimensional phase is reached as well. A quasi-2D structure with $n = 2$ forms in the bottom part of the film, with the inorganic slabs parallel to the substrate and the PEA molecules perpendicularly oriented. The mechanism of formation of the studied RDP Sn-based perovskite films is depicted schematically in the last two rows of Figure 4. Predominant crystallization in the form of pure $FASnI_3$ on the first growing nuclei may also be the consequence of the higher affinity of the FA^+ cations to the $[SnI_6]^{4-}$ octahedron with respect to PEA^+.[54] Indeed, the energy of formation of the 3D structure is expected to be smaller than the 2D phase, if one consider the higher stability of the 3D phase ($T_m > T_d \approx 335$ °C, where T_m and T_d stand for melting temperature and decomposition temperature, respectively) with respect to the 2D phase ($T_m > T_d \approx 213$ °C).[55,56]

Finally, having unveiled the mechanism of formation of these tin-based RDP perovskite thin films, we aim now to make a correlation between the final film structure and the solar cell device performances. The PCE is plotted in **Figure 5** against the *n* number. The pure 3D material shows a PCE of about 6%.[57] This PCE is significantly improved by addition of a small quantity of the 2D component. The highest PCE value around 9.0% was achieved for the device prepared with $n = 24$.[21] This remarkable PCE improvement is related to the oriented 3D crystalline structure induced by the addition of the low-dimensional component via suppression of the bulk crystallization and stabilization of the crystal orientation through the solution crystallization process, according to what we have commented above (see Figure 1; Figure S9, Supporting Information). The PCE of the solar cell drops when more 2D component is present in the perovskite film ($n \leq 16$) though the orientation of the high *n* phases increase. The GIWAXS patterns (see Figure S9 in the Supporting Information) of these films prepared using exactly the same conditions as those used for the solar cells reveals a significant larger amount of parallel orientated $n = 2$ phase at the bottom than that of $n = 24$, also in agreement with the in situ results (Figure 4). In this case, the large amount of $n = 2$ phase hinders the charge transport and collection in the solar cell (Figure S9, Supporting Information). It is also important to underline that next to the crystallinity also the film morphology plays an important role and solar cells, and the appearance of films inhomogeneities can be highly detrimental for device performances.

3. Conclusion

In summary, we have studied the structural transformations occurring in the formation of pure 3D $FASnI_3$, pure 2D PEA_2SnI_4, and RDP hybrid $PEA_2FA_{n-1}Sn_nI_{3n+1}$ thin films during spin coating at ambient temperature and over a wide range of *n*. On the basis of our ex situ and in situ GIWAXS results, together with SEM microscopy and photoluminescence spectroscopy, we can draw several important conclusions. i) For Sn-based perovskites processed by spin coating from DMF:DMSO solution, the crystalline perovskite phase is formed directly from a disordered precursor solution. ii) Crystallization always tends to start at the air/solution interface. iii) In the pure 3D solution and in the 2D/3D mixed solutions with $n > 24$, the rate of crystal growth in the bulk of the solution is comparable to the one at the air/solution interface. iv) In the solutions of the pure 2D material and with $n \leq 24$, bulk crystallization is negligible. v) The presence of the PEA^+ molecules in the precursor solution seems to be responsible for the suppression of the bulk crystallization and leads to a change in the growth mode of the perovskite crystalline film, assisting the growth of a highly oriented top layer with crystal structure similar to the 3D phase. vi) The bottom part of the film, especially for $n \leq 16$, in contact with the substrate is occupied by a quasi-2D RDP phase with $n = 2$ that grows parallel to the substrate and is the last one to crystallize. The structure of this quasi-2D phase is independent of the nominal amount of 2D component added to the initial solution and is present in every investigated hybrid sample, reflecting its thermodynamic stability.

Our data highlight the difference between the Sn- and Pb-based perovskites, especially in the sequence of precursors and intermediate phases involved in the thin film crystal formation process. More efforts should be certainly focused to understand the nature of these disordered colloidal precursors in Sn halide solutions, facing the challenge of their fast evolution into the crystalline state. Further control of the growth and orientation of not only the top phase, but also of the bottom phase

in contact with the substrate will be required in the future to achieve higher performances. We hope that this contribution may be an inspiration for researchers in Sn-based perovskites and can pave the way to develop more stable PSCs with better PCE properties through the knowledge of the fundamental aspects of crystal formation from precursor solutions.

Supporting Information

Supporting Information is available from the Wiley Online Library or from the author.

Acknowledgements

J.D. and S.S. contributed equally to this work. The ESRF and NWO are acknowledged for allocating the beam time at the Dutch-Belgian beamline (DUBBLE, ESRF, Grenoble) for the GIWAXS experiments. The authors are grateful to the DUBBLE team for their help during the beam time. Loredana Protesescu and Graeme Blake are acknowledged for insightful discussions about the paper. S.K. is thankful for a research fellowship (Grant No. 408012143) awarded by the Deutsche Forschungsgemeinschaft (DFG). G.P. acknowledges the Zernike Institute for Advanced Materials for the startup funds. J.D. and G.P. are grateful to the China Scholarship Council.

Conflict of Interest

The authors declare no conflict of interest.

Keywords

crystal orientation, film formation mechanism, in situ GIWAXS, Ruddlesden–Popper, spin coating, tin perovskite solar cells

Received: February 11, 2020
Published online: March 31, 2020

[1] A. Kojima, K. Teshima, Y. Shirai, T. Miyasaka, *J. Am. Chem. Soc.* **2009**, *131*, 6050.
[2] G. Xing, N. Mathews, S. Sun, S. S. Lim, Y. M. Lam, M. Grätzel, S. Mhaisalkar, T. C. Sum, *Science* **2013**, *342*, 344.
[3] S. D. Stranks, G. E. Eperon, G. Grancini, C. Menelaou, M. J. P. Alcocer, T. Leijtens, L. M. Herz, A. Petrozza, H. J. Snaith, *Science* **2013**, *342*, 341.
[4] C. Wehrenfennig, G. E. Eperon, M. B. Johnston, H. J. Snaith, L. M. Herz, *Adv. Mater.* **2014**, *26*, 1584.
[5] M. M. Lee, J. Teuscher, T. Miyasaka, T. N. Murakami, H. J. Snaith, *Science* **2012**, *338*, 643.
[6] H.-S. Kim, C.-R. Lee, J.-H. Im, K.-B. Lee, T. Moehl, A. Marchioro, S.-J. Moon, R. Humphry-Baker, J.-H. Yum, J. E. Moser, M. Grätzel, N.-G. Park, *Sci. Rep.* **2012**, *2*, 591.
[7] J. Burschka, N. Pellet, S.-J. Moon, R. Humphry-Baker, P. Gao, M. K. Nazeeruddin, M. Grätzel, *Nature* **2013**, *499*, 316.
[8] S. Shao, J. Liu, H.-H. Fang, L. Qiu, G. H. ten Brink, J. C. Hummelen, L. J. A. Koster, M. A. Loi, *Adv. Energy Mater.* **2017**, *7*, 1701305.
[9] S. Shao, M. Abdu-Aguye, T. S. Sherkar, H.-H. Fang, S. Adjokatse, G. ten Brink, B. J. Kooi, L. J. A. Koster, M. A. Loi, *Adv. Funct. Mater.* **2016**, *26*, 8094.
[10] S. Shao, Z. Chen, H. H. Fang, G. H. Ten Brink, D. Bartesaghi, S. Adjokatse, L. J. A. Koster, B. J. Kooi, A. Facchetti, M. A. Loi, *J. Mater. Chem. A* **2016**, *4*, 2419.
[11] Best Research-Cell Efficiency Chart | Photovoltaic Research | NREL, https://www.nrel.gov/pv/cell-efficiency.html (accessed: December 2019).
[12] W. Xiang, W. Tress, *Adv. Mater.* **2019**, *31*, 1902851.
[13] C. C. Stoumpos, C. D. Malliakas, M. G. Kanatzidis, *Inorg. Chem.* **2013**, *52*, 9019.
[14] M. H. Kumar, S. Dharani, W. L. Leong, P. P. Boix, R. R. Prabhakar, T. Baikie, C. Shi, H. Ding, R. Ramesh, M. Asta, M. Graetzel, S. G. Mhaisalkar, N. Mathews, *Adv. Mater.* **2014**, *26*, 7122.
[15] S. Shao, J. Dong, H. Duim, G. H. ten Brink, G. R. Blake, G. Portale, M. A. Loi, *Nano Energy* **2019**, *60*, 810.
[16] M. Jung, S.-G. Ji, G. Kim, S. Il Seok, *Chem. Soc. Rev.* **2019**, *48*, 2011.
[17] J. Seo, J. H. Noh, S. Il Seok, *Acc. Chem. Res.* **2016**, *49*, 562.
[18] L. Protesescu, S. Yakunin, M. I. Bodnarchuk, F. Krieg, R. Caputo, C. H. Hendon, R. X. Yang, A. Walsh, M. V Kovalenko, *Nano Lett.* **2015**, *15*, 3692.
[19] H. Tsai, W. Nie, J.-C. Blancon, C. C. Stoumpos, R. Asadpour, B. Harutyunyan, A. J. Neukirch, R. Verduzco, J. J. Crochet, S. Tretiak, L. Pedesseau, J. Even, M. A. Alam, G. Gupta, J. Lou, P. M. Ajayan, M. J. Bedzyk, M. G. Kanatzidis, A. D. Mohite, *Nature* **2016**, *536*, 312.
[20] S. Kahmann, S. Shao, M. A. Loi, *Adv. Funct. Mater.* **2019**, *29*, 1902963.
[21] S. Shao, J. Liu, G. Portale, H.-H. Fang, G. R. Blake, G. H. ten Brink, L. J. A. Koster, M. A. Loi, *Adv. Energy Mater.* **2018**, *8*, 1702019.
[22] P. Pistor, J. Borchert, W. Fränzel, R. Csuk, R. Scheer, *J. Phys. Chem. Lett.* **2014**, *5*, 3308.
[23] J. Schlipf, P. Müller-Buschbaum, *Adv. Energy Mater.* **2017**, *7*, 1700131.
[24] Q. Hu, L. Zhao, J. Wu, K. Gao, D. Luo, Y. Jiang, Z. Zhang, C. Zhu, E. Schaible, A. Hexemer, C. Wang, Y. Liu, W. Zhang, M. Grätzel, F. Liu, T. P. Russell, R. Zhu, Q. Gong, *Nat. Commun.* **2017**, *8*, 15688.
[25] C. Lin, S. Li, J. Chang, H. Chia, Y. Hsiao, C. Su, B. Lian, C. Wen, S. Huang, W. Wu, D. Wang, A. Su, C. Chen, U. Jeng, *Adv. Funct. Mater.* **2019**, *29*, 1902582.
[26] R. Szostak, P. E. Marchezi, A. D. S. Marques, J. C. Da Silva, M. S. De Holanda, M. M. Soares, H. C. N. Tolentino, A. F. Nogueira, *Sustainable Energy Fuels* **2019**, *3*, 2287.
[27] O. Filonik, M. E. Thordardottir, J. Lebert, S. Pröller, S. Weiß, L. J. Haur, A. Priyadarshi, P. Fontaine, P. Müller-Buschbaum, N. Mathews, E. M. Herzig, *Energy Technol.* **2019**, *7*, 1900343.
[28] H. Tsai, R. Asadpour, J.-C. Blancon, C. C. Stoumpos, O. Durand, J. W. Strzalka, B. Chen, R. Verduzco, P. M. Ajayan, S. Tretiak, J. Even, M. A. Alam, M. G. Kanatzidis, W. Nie, A. D. Mohite, *Science* **2018**, *360*, 67.
[29] A. Z. Chen, M. Shiu, J. H. Ma, M. R. Alpert, D. Zhang, B. J. Foley, D.-M. Smilgies, S.-H. Lee, J. J. Choi, *Nat. Commun.* **2018**, *9*, 1336.
[30] J. Qiu, Y. Xia, Y. Zheng, W. Hui, H. Gu, W. Yuan, H. Yu, L. Chao, T. Niu, Y. Yang, X. Gao, Y. Chen, W. Huang, *ACS Energy Lett.* **2019**, *4*, 1513.
[31] D. S. Lee, J. S. Yun, J. Kim, A. M. Soufiani, S. Chen, Y. Cho, X. Deng, J. Seidel, S. Lim, S. Huang, A. W. Y. Ho-Baillie, *ACS Energy Lett.* **2018**, *3*, 647.
[32] Y. Hu, J. Schlipf, M. Wussler, M. L. Petrus, W. Jaegermann, T. Bein, P. Müller-Buschbaum, P. Docampo, *ACS Nano* **2016**, *10*, 5999.
[33] Y. Liao, H. Liu, W. Zhou, D. Yang, Y. Shang, Z. Shi, B. Li, X. Jiang, L. Zhang, L. N. Quan, R. Quintero-Bermudez, B. R. Sutherland, Q. Mi, E. H. Sargent, Z. Ning, *J. Am. Chem. Soc.* **2017**, *139*, 6693.
[34] C. M. M. Soe, G. P. Nagabhushana, R. Shivaramaiah, H. Tsai, W. Nie, J.-C. Blancon, F. Melkonyan, D. H. Cao, B. Traoré, L. Pedesseau, M. Kepenekian, C. Katan, J. Even, T. J. Marks, A. Navrotsky, A. D. Mohite, C. C. Stoumpos, M. G. Kanatzidis, *Proc. Natl. Acad. Sci.* **2019**, *116*, 58.

[35] S. Paek, P. Schouwink, E. N. Athanasopoulou, K. T. Cho, G. Grancini, Y. Lee, Y. Zhang, F. Stellacci, M. K. Nazeeruddin, P. Gao, *Chem. Mater.* **2017**, *29*, 3490.
[36] F. Wang, X. Jiang, H. Chen, Y. Shang, H. Liu, J. Wei, W. Zhou, H. He, W. Liu, Z. Ning, *Joule* **2018**, *2*, 2732.
[37] G. Fleury, D. Hermida-Merino, D. Jingjin, K. Aissou, A. Bytchkov, G. Portale, *Adv. Funct. Mater.* **2019**, *29*, 1806741.
[38] J. J. van Franeker, D. Hermida-Merino, C. Gommes, K. Arapov, J. J. Michels, R. A. J. Janssen, G. Portale, *Adv. Funct. Mater.* **2017**, *27*, 1702516.
[39] Y. Zhang, P. Wang, M.-C. Tang, D. Barrit, W. Ke, J. Liu, T. Luo, Y. Liu, T. Niu, D.-M. Smilgies, Z. Yang, Z. Liu, S. Jin, M. G. Kanatzidis, A. Amassian, S. F. Liu, K. Zhao, *J. Am. Chem. Soc.* **2019**, *141*, 2684.
[40] X. Zhang, R. Munir, Z. Xu, Y. Liu, H. Tsai, W. Nie, J. Li, T. Niu, D.-M. Smilgies, M. G. Kanatzidis, A. D. Mohite, K. Zhao, A. Amassian, S. F. Liu, *Adv. Mater.* **2018**, *30*, 1707166.
[41] Y. Bai, S. Xiao, C. Hu, T. Zhang, X. Meng, Q. Li, Y. Yang, K. S. Wong, H. Chen, S. Yang, *Nano Energy* **2017**, *34*, 58.
[42] N. J. Jeon, J. H. Noh, Y. C. Kim, W. S. Yang, S. Ryu, S. Il Seok, *Nat. Mater.* **2014**, *13*, 897.
[43] R. Munir, A. D. Sheikh, M. Abdelsamie, H. Hu, L. Yu, K. Zhao, T. Kim, O. El Tall, R. Li, D.-M. Smilgies, A. Amassian, *Adv. Mater.* **2017**, *29*, 1604113.
[44] T. Yokoyama, D. H. Cao, C. C. Stoumpos, T.-B. Song, Y. Sato, S. Aramaki, M. G. Kanatzidis, *J. Phys. Chem. Lett.* **2016**, *7*, 776.
[45] D. T. W. Toolan, A. Isakova, R. Hodgkinson, N. Reeves-McLaren, O. S. Hammond, K. J. Edler, W. H. Briscoe, T. Arnold, T. Gough, P. D. Topham, J. R. Howse, *Macromolecules* **2016**, *49*, 4579.
[46] M. Avrami, *J. Chem. Phys.* **1941**, *9*, 177.
[47] M. Avrami, *J. Chem. Phys.* **1940**, *8*, 212.
[48] M. Avrami, *J. Chem. Phys.* **1939**, *7*, 1103.
[49] B. J. Kooi, *Phys. Rev. B* **2006**, *73*, 054103.
[50] S. F. Hulbert, J. J. Klawitter, *J. Am. Ceram. Soc.* **1967**, *50*, 484.
[51] Y. Lin, Y. Fang, J. Zhao, Y. Shao, S. J. Stuard, M. M. Nahid, H. Ade, Q. Wang, J. E. Shield, N. Zhou, A. M. Moran, J. Huang, *Nat. Commun.* **2019**, *10*, 1008.
[52] A. A. Zhumekenov, V. M. Burlakov, M. I. Saidaminov, A. Alofi, M. A. Haque, B. Turedi, B. Davaasuren, I. Dursun, N. Cho, A. M. El-Zohry, M. De Bastiani, A. Giugni, B. Torre, E. Di Fabrizio, O. F. Mohammed, A. Rothenberger, T. Wu, A. Goriely, O. M. Bakr, *ACS Energy Lett.* **2017**, *2*, 1782.
[53] T. M. Koh, V. Shanmugam, X. Guo, S. S. Lim, O. Filonik, E. M. Herzig, P. Müller-Buschbaum, V. Swamy, S. T. Chien, S. G. Mhaisalkar, N. Mathews, *J. Mater. Chem. A* **2018**, *6*, 2122.
[54] W. S. Yang, J. H. Noh, N. J. Jeon, Y. C. Kim, S. Ryu, J. Seo, S. Il Seok, *Science* **2015**, *348*, 1234.
[55] T. Li, A. M. Zeidell, G. Findik, W. A. Dunlap-Shohl, J. Euvrard, K. Gundogdu, O. D. Jurchescu, D. B. Mitzi, *Chem. Mater* **2019**, *31*, 36.
[56] W. Ke, C. C. Stoumpos, M. Zhu, L. Mao, I. Spanopoulos, J. Liu, O. Y. Kontsevoi, M. Chen, D. Sarma, Y. Zhang, M. R. Wasielewski, M. G. Kanatzidis, *Sci. Adv.* **2017**, *3*, e1701293.
[57] M. Konstantakou, T. Stergiopoulos, *J. Mater. Chem. A* **2017**, *5*, 11518.